Collective cell migration requires vesicular trafficking for chemoattractant delivery at the trailing edge

Paul W. Kriebel,[1] Valarie A. Barr,[1] Erin C. Rericha,[1,3] Guofeng Zhang,[2] and Carole A. Parent[1]

[1]Laboratory of Cellular and Molecular Biology, National Cancer Institute, and [2]Division of Bioengineering and Physical Sciences, National Institute of Biomedical Imaging and Bioengineering, National Institutes of Health, Bethesda, MD 20892
[3]Institute for Research in Electronics and Applied Physics, University of Maryland, College Park, MD 20742

Chemoattractant signaling induces the polarization and directed movement of cells secondary to the activation of multiple effector pathways. In addition, chemotactic signals can be amplified and relayed to proximal cells via the synthesis and secretion of additional chemoattractant. The mechanisms underlying such remarkable features remain ill defined. We show that the asymmetrical distribution of adenylyl cyclase (ACA) at the back of *Dictyostelium discoideum* cells, an essential determinant of their ability to migrate in a head-to-tail fashion, requires vesicular trafficking. This trafficking results in a local accumulation of ACA-containing intracellular vesicles and involves intact actin, microtubule networks, and de novo protein synthesis. We also show that migrating cells leave behind ACA-containing vesicles, likely secreted as multivesicular bodies and presumably involved in the formation of head-to-tail arrays of migrating cells. We propose that similar compartmentalization and shedding mechanisms exist in mammalian cells during embryogenesis, wound healing, neuron growth, and metastasis.

Introduction

A wide variety of cells have the ability to sense and migrate directionally along external gradients of chemoattractants. This process, called chemotaxis, is fundamental for a multitude of physiological processes including embryogenesis, angiogenesis, and wound healing. It is also important in the pathophysiology of asthma, arthritis, and metastatic invasion (Ridley et al., 2003). Upon exposure to a chemoattractant gradient, cells polarize, orient themselves, and migrate directionally. In this context, fast moving neutrophils and *Dictyostelium discoideum* cells are in a league of their own (Parent, 2004). These cells have the ability to sense extremely shallow chemoattractant gradients and quickly transduce them into highly polarized cellular responses, where F-actin is highly enriched at the front for pseudopod extension and myosin II is mainly assembled at the back for contraction and retraction. For both neutrophils and *Dictyostelium*, chemoattractants mediate their effects by binding to seven transmembrane, G protein–coupled receptors. Activation of the receptors leads to dissociation of heterotrimeric G proteins into Gα and Gβγ subunits and activation of multiple downstream effectors that ultimately give rise to cell polarity and migration (Van Haastert and Devreotes, 2004; Affolter and Weijer, 2005; Bagorda et al., 2006).

Dictyostelium has been invaluable to decipher the signal transduction mechanisms regulating chemotaxis (Kimmel and Parent, 2003; Franca-Koh et al., 2006). Upon starvation, these cells rely on chemotaxis to locate and migrate toward each other and form an aggregate that will differentiate into a multicellular organism. Remarkably, as the cells polarize and migrate directionally to form the aggregate, they do so by aligning in a head-to-tail fashion, forming characteristic chains of cells or streams. The ability of *Dictyostelium* cells to spontaneously aggregate and stream relies on the presence of an exquisitely regulated signal relay loop that is centered on cAMP. In this organism, the detection, synthesis, and degradation of cAMP are highly regulated (Kriebel and Parent, 2004). The addition of chemoattractants leads to a burst in the activity of adenylyl cyclase (ACA),

Correspondence to Carole A. Parent: parentc@mail.nih.gov

Abbreviations used in this paper: ACA, adenylyl cyclase; cAR, cAMP receptor; CHC, clathrin heavy chain; CHX, cycloheximide; CLC, clathrin light chain; CRAC, cytosolic regulator of ACA; LatA, latrunculin A; MTOC, microtubule organizing center; MVB, multivesicular body; MyoJ, myosin J; Noco, Nocodazole; PI3K, phosphatidylinositol-3-kinase; ROI, region of interest; WT, wild type.

The online version of this article contains supplemental material.

The Rockefeller University Press $30.00
J. Cell Biol. Vol. 183 No. 5 949–961
www.jcb.org/cgi/doi/10.1083/jcb.200808105

which converts ATP into cAMP. Most of the cAMP produced is secreted and acts as a chemoattractant by binding to specific G protein–coupled receptors exposed at the cell surface (cAMP receptors [cARs]; Parent and Devreotes, 1996b). Receptor stimulation leads to the activation of a variety of effectors, including ACA, which amplifies and relays the signal to neighboring cells. Finally, the extracellular concentration of cAMP is tightly controlled through the expression of membrane-bound and secreted forms of a phosphodiesterase and a specific phosphodiesterase inhibitor, allowing the signaling cascade to come back to basal levels and respond to further stimulation (Franke and Kessin, 1992).

We previously showed that transmission of chemotactic signals to neighboring cells is a spatially regulated process. When exposed to an external point source of cAMP, cells lacking ACA can migrate directionally but cannot relay the chemotactic signal to neighboring cells or align in a head-to-tail fashion to form streams. This streaming behavior not only depends on the presence of ACA but, most remarkably, on its enrichment at the back of polarized cells (Kriebel et al., 2003). We proposed that the asymmetrical distribution of ACA provides a compartment from which cAMP is locally released to attract neighboring cells to the back of cells ahead of them. We now report that vesicle trafficking on microtubules is required for the enrichment of ACA at the back of cells. Remarkably, we also establish that ACA-containing vesicles are shed at the back of migrating cells and that de novo ACA synthesis is essential to maintain the cellular distribution of ACA. Together, these findings showcase the mechanisms regulating the asymmetrical distribution of proteins in polarized cells and the controlled release of chemoattractants.

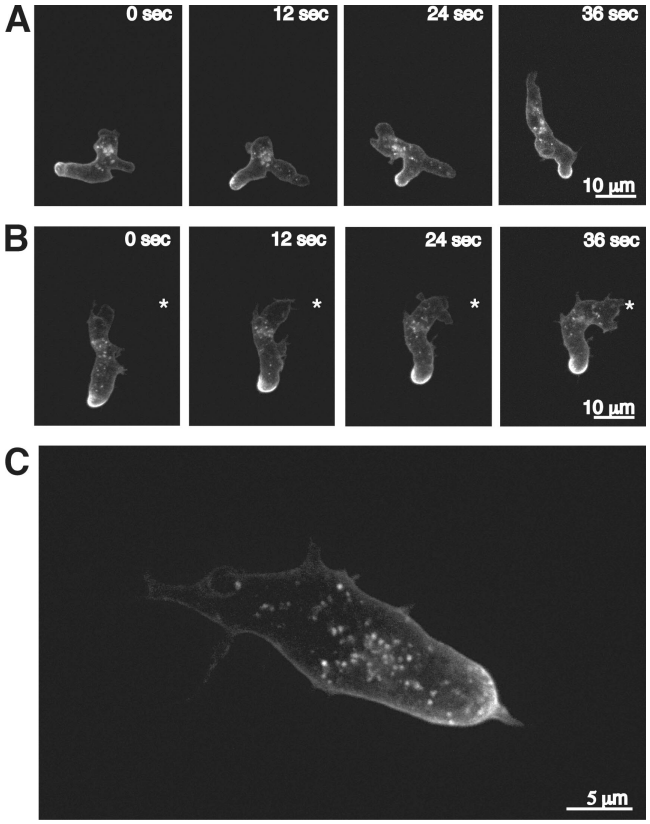

Figure 1. **ACA is localized on dynamic vesicles that coalesce at the back of polarized cells.** (A) Montage of fluorescent images showing maximum intensity projections of a randomly moving ACA-YFP/*aca*$^-$ cell. Also see Video 1. (B) Montage of fluorescent images showing maximum intensity projections of a ACA-YFP/*aca*$^-$ cell chemotaxing toward a micropipette filled with 1 μM cAMP. The asterisk depicts the position of the micropipette. Also see Video 1. (C) 3D reconstruction of z-stack slices showing accumulation of vesicles at the back of a migrating ACA-YFP/*aca*$^-$ cell. Also see Video 2. Videos are available at http://www.jcb.org/cgi/content/full/jcb.200808105/DC1.

Results

Enrichment of ACA at the back of migrating cells depends on an intracellular pool of the enzyme

We used confocal microscopy to better define the partitioning of ACA in fully differentiated ACA-YFP/*aca*$^-$ cells. Fig. 1 A shows images of maximum intensity projections from a randomly migrating cell. There is a clear enrichment of ACA at the back of cells as well as the uniform staining at the cell periphery. In addition, ACA is seen on intracellular vesicles that move very rapidly across the cytoplasm (Video 1, available at http://www.jcb.org/cgi/content/full/jcb.200808105/DC1). Closer examination reveals that most vesicles are moving back and forth from a perinuclear aggregation center to the back of cells, whereas a smaller subset of solitary vesicles reach extending pseudopods. The same phenomenon is observed in cells subjected to a point source of chemoattractant (Fig. 1 B and Video 1). Upon closer examination, we observe that the ACA-enriched region at the back of cells corresponds to a dense accumulation of labeled vesicles, a phenomenon that is clearly substantiated by visualization of 3D reconstructions from confocal z stacks (Fig. 1 C and Video 2).

We next used FRAP to define the mechanisms responsible for establishing the asymmetrical distribution of ACA. In these experiments we photobleached part of the cell periphery and carefully monitored the fluorescence recovery over time. We reasoned that if the recovery is solely dependent on membrane diffusion, it should proceed in a vectorial fashion from the adjacent unbleached areas. Conversely, if replenishment involves an intracellular pool of ACA, we should measure an even fluorescence recovery in the middle and the boundaries of the bleached zone (Fig. 2 A). We optimized our FRAP conditions to study the recovery of ACA over a large portion of the plasma membrane for long periods of time. To reduce photodamage, we captured images every 45 s, which precluded us from obtaining quantitative diffusion measurements. As a control for these experiments, we used cells expressing the seven-transmembrane chemoattractant cAR1 fused to YFP, which is uniformly distributed on the plasma membrane and does not localize to intracellular vesicles (Xiao et al., 1997). Differentiated cells were plated at very low density, allowing them to become apolar (Kriebel et al., 2003), and a small region of the cell periphery was bleached. As depicted in Fig. 2 B, we find a dramatic difference in the fluorescence recovery patterns of the cAR1-YFP/*car1*$^{/3-}$ and ACA-YFP/*aca*$^-$ cells. Whereas the receptor shows a recovery pattern reminiscent of membrane

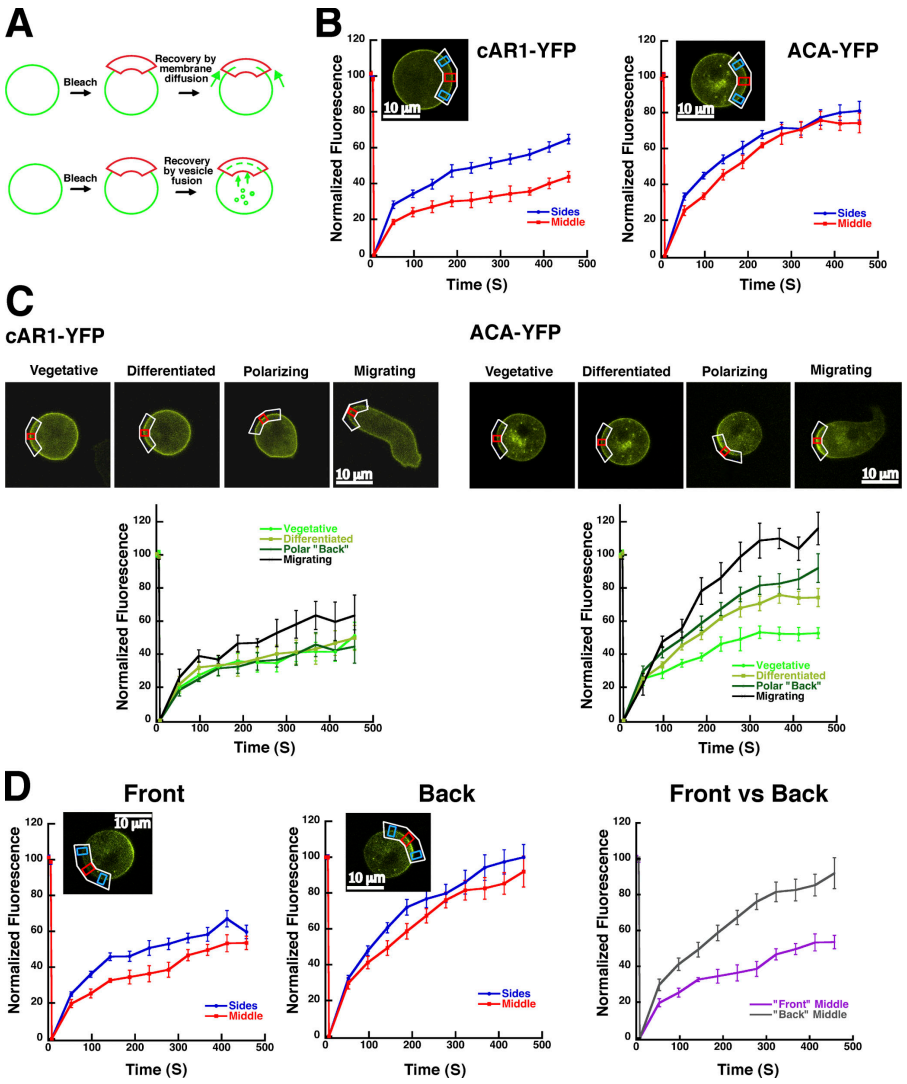

Figure 2. **FRAP analyses reveal a role for vesicle trafficking in the asymmetrical distribution of ACA.** (A) Cartoon depicting the potential effect of intracellular vesicles on the fluorescence recovery pattern after photobleaching. (B, inset) Confocal fluorescent images of cAR1-YFP/*car1/3*$^-$ cells (left) and ACA-YFP/*aca*$^-$ cells (right) showing the bleached area (white) and the side (blue) and middle (red) boxes where the fluorescence recovery is monitored. The graphs depict the recovery of ACA-YFP and cAR1-YFP from differentiated nonpolar cells. The side fluorescence recovery values are shown in blue and the middle recovery values are in red. Each graph is normalized by setting initial fluorescence to 100% and the fluorescence immediately after bleaching to 0. Data are presented as a mean of five cells ± SEM. (C, top) Confocal fluorescent images of vegetative, differentiated nonpolar, polar, and migrating cAR1-YFP/*car1/3*$^-$ (left) and ACA-YFP/*aca*$^-$ (right) cells showing the bleached area in white and a red box where the fluorescence recovery is monitored. (bottom) Graphs depicting the fluorescence recovery of cAR1-YFP (left) and ACA-YFP (right) in the middle boxes (red) in vegetative, differentiated nonpolar, polar, and migrating cells. Data are presented as a mean of five cells ± SEM. (D, inset) Confocal fluorescent images of a ACA-YFP/*aca*$^-$ polar cell showing the bleached area as in B. The graphs depict the recovery of ACA-YFP at the front (left) and back (right) of a polarized cell. See B for details. The front versus back graph compares the recovery from the middle box (red) at the front and the back, respectively.

diffusion, ACA displays a uniform recovery throughout the bleached region. Replenishment of ACA at the cell periphery thus proceeds from an intracellular location.

To gain further insight into the mechanism of fluorescence recovery, FRAP analyses were performed on vegetative cells and on cells in various stages of polarization. We observe that as ACA-YFP–expressing cells enter development, polarize, and become motile, the extent of the fluorescence recovery dramatically increases (Fig. 2 C). In sharp contrast, the recovery of cAR1-YFP–expressing cells does not significantly change during development and polarization, although we noticed a consistent increase in the extent of recovery in migrating cAR1-YFP cells (Fig. 2 C). We envision that this is secondary to the highly dynamic state of migrating cells. Importantly, when we compare the ACA-YFP recovery pattern at the front and back of differentiated polar cells, we observe a dramatic difference, where the back recovers earlier and to a greater extent than the front (Fig. 2 D). Together these findings show that the machinery controlling the asymmetrical distribution of ACA-YFP is developmentally regulated. Along with our earlier findings (Fig. 1), these observations suggest that vesicle trafficking plays a key role in the enrichment of ACA at the back of polarized cells.

F-actin and microtubules control the enrichment of ACA at the back of cells

The association of ACA with intracellular vesicles (Fig. 1) and its rapid, differentiation-dependent replenishment at the cell membrane (Fig. 2) suggest a role for the cytoskeleton in ACA trafficking. To determine the role of the actin cytoskeleton on these processes, we treated differentiated ACA-YFP/*aca*$^-$ cells with 5 μM latrunculin A (LatA) and monitored the distribution of the ACA-containing vesicles with time. As we previously reported, LatA-treated cells rapidly round-up and stop moving, and the distribution of ACA on the cell periphery concomitantly becomes uniform (Fig. 3 A; Kriebel et al., 2003). However, within 45 min after the addition of LatA, the ACA-positive vesicles disappear and cells show a very bright ACA signal at their periphery (Fig. 3 A), a response that we also readily observe when we treat cells with 60 μM LatA for 5 min (not depicted). When LatA-treated cells are photobleached as described in Fig. 2, recovery of the ACA signal now mimics the membrane diffusion pattern of the cAR1 cells, with the side boxes recovering before the middle box (Fig. 3 A; LatA-treated cAR1-YFP cells showed an identical response [not depicted]). This treatment also markedly reduced the ability of chemoattractants to stimulate ACA activity (Fig. S1, available

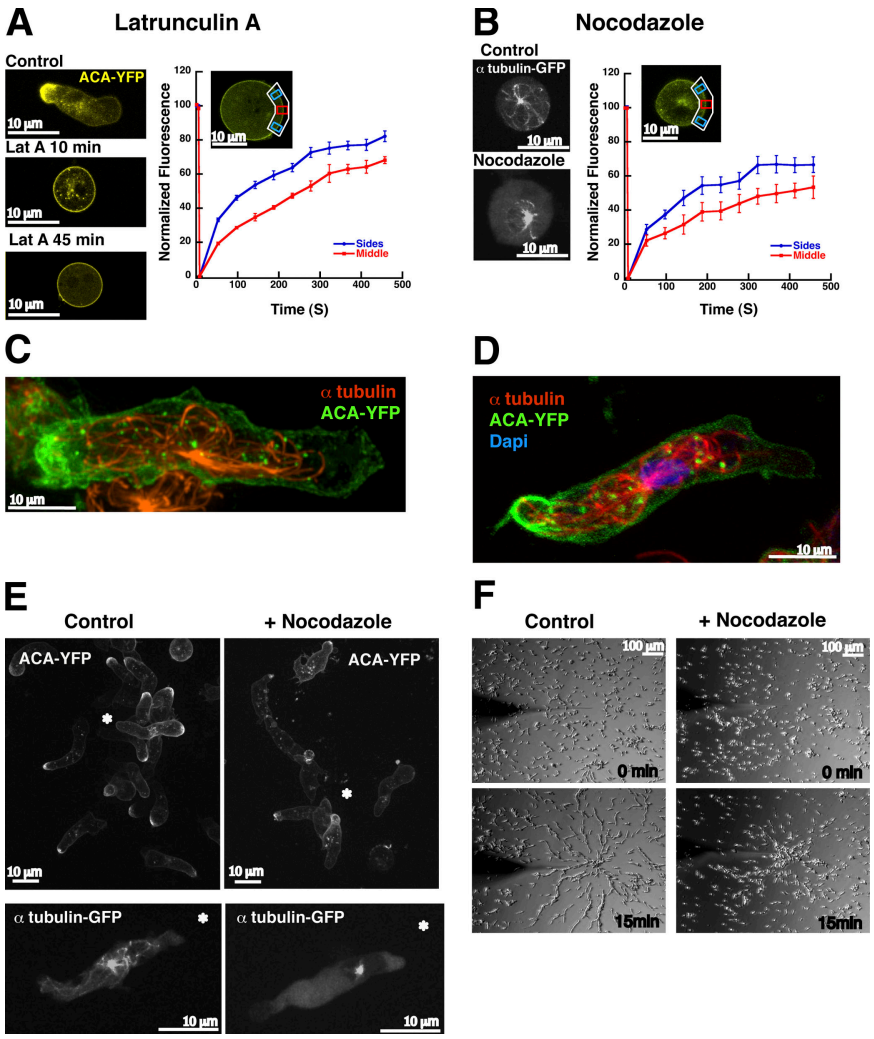

Figure 3. **F-actin and microtubules control the enrichment of ACA at the back of cells.** (A, left) Confocal fluorescent images of ACA-YFP/*aca*⁻ cells treated with 5 μM LatA for the designated lengths of time. (inset) Confocal fluorescent image of an ACA-YFP/*aca*⁻ cell treated with LatA for 45 min showing the bleached area (white) and the side (blue) and middle (red) boxes where the fluorescence recovery is monitored. The graphs depict the recovery of ACA-YFP. Data is presented as a mean of five cells ± SEM. See Fig. 2 B for details. (B, left) Fluorescent images of GFP–α-tubulin/WT cells with or without 60 μM Noco. (inset) Confocal fluorescent image of an ACA-YFP/*aca*⁻ cell treated with Noco showing the bleached area. The graphs depict the recovery of ACA-YFP. Data is presented as a mean of five cells ± SEM. See Fig. 2 B for details. (C) Deconvoluted fluorescent image showing ACA-YFP (green) and α-tubulin (red) in fixed ACA-YFP/*aca*⁻ cells. Also see Video 3. (D) Fluorescent image showing ACA-YFP (green), α-tubulin (red), and DAPI (blue) in fixed ACA-YFP/*aca*⁻ cells. The position of the MTOC relative to the nucleus was quantified in 63 cells. We find that in 62% of migrating cells the MTOC is localized behind the nucleus and that 76% of cells have either none or one microtubule filament extending to the leading edge. The position of the MTOC was confirmed by labeling centrosomes with anti–γ-tubulin antibodies (not depicted). (E) Fluorescent maximum intensity projections of ACA-YFP/*aca*⁻ cells (top) or GFP–α-tubulin/WT cells (bottom) chemotaxing to a micropipette filled with 1 μM cAMP in the presence or absence of Noco. The asterisk shows the position of the micropipette. (F) Montage of bright field images of ACA-YFP/*aca*⁻ cells chemotaxing to a micropipette filled with 1 μM cAMP in the presence or absence of Noco. Also see Video 4. Identical results were observed with WT cells. Videos are available at http://www.jcb.org/cgi/content/full/jcb.200808105/DC1.

at http://www.jcb.org/cgi/content/full/jcb.200808105/DC1). Conversely, the chemoattractant-mediated translocation of PH_{CRAC}-GFP to the plasma membrane is unaffected under these conditions (Fig. S2), indicating that LatA treatment had no generalized detrimental effects on cAR1-mediated signal transduction pathways. These findings show that actin-dependent processes are required to maintain the asymmetrical enrichment of ACA at the cell periphery.

We next studied the role of microtubules on ACA vesicle trafficking using Nocodazole (Noco) treatment. For these experiments, we monitored the effects of Noco using cells expressing GFP–α-tubulin (Neujahr et al., 1998) and found that treating cells with 60 μM Noco for 1 h causes a substantial disassembly of the microtubule network (Fig. 3 B). Under these conditions, differentiated ACA-YFP/*aca*⁻ change their shape, with a majority of cells losing their polarity and appearing round or slightly oblong. Simultaneously, the distribution of ACA-YFP on the cell periphery becomes uniform (Fig. 3 B, inset). Most interestingly, the recovery of the ACA-YFP signal after photobleaching again mimics the membrane diffusion pattern of the cAR1-YFP cells, with the side boxes recovering before the middle box (Fig. 3 B; Noco treatment had no effect on the fluorescent recovery of cAR1-YFP cells [not depicted]). These findings indicate that an intact microtubule network is required for the asymmetrical enrichment of ACA at the cell periphery.

We next set out to determine if ACA vesicles are associated with microtubules. We fixed fully differentiated ACA-YFP/*aca*⁻ cells, stained them with an anti–α-tubulin antibody, and performed deconvolution microscopy. As expected, we find that the ACA vesicles align on microtubules (Fig. 3 C and Video 3, available at http://www.jcb.org/cgi/content/full/jcb.200808105/DC1). Upon further analyses, we discovered that the front of polarized cells is virtually devoid of ACA vesicles and microtubules, although ACA is clearly present around the entire cell periphery and may appear spotty especially at the leading edge. Indeed, quantitative analyses show that in 62% of migrating cells (n = 63) the microtubule organizing center (MTOC) is localized behind the nucleus where an intricate microtubule network emanates toward the back of every cell. In contrast, 76% of the cells have either none or one microtubule filament extending to their leading edge (Fig. 3 D). These findings suggest that the microtubule network is organized to promote the trafficking of cargo, including ACA, to and from the back of highly polarized cells. In support of this notion, we find that Noco-treated ACA-YFP/*aca*⁻ cells exposed to a chemoattractant-containing micropipette polarize and migrate rapidly but show a significant defect

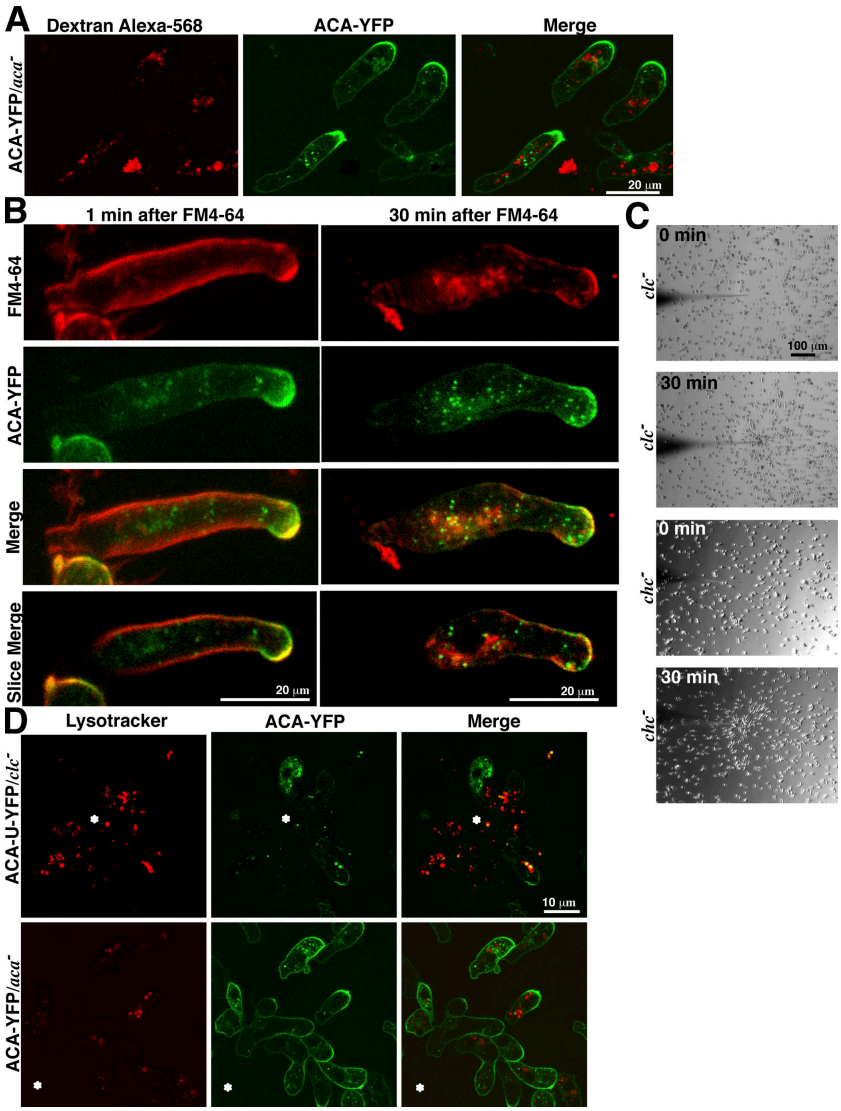

Figure 4. **ACA vesicles are not targeted to lysosomes and require proper assembly of clathrin for trafficking.** (A) Montage of confocal fluorescent images depicting Dextran–Alexa 568 (red) and ACA-YFP (green) distribution in ACA-YFP/*aca*$^-$ cells. (B) Spinning disk and confocal fluorescent images of ACA-YFP/*aca*$^-$ cells labeled with FM4-64 (red) for 1 and 30 min and ACA-YFP (green). In the top six images, maximum intensity projections are presented. The bottom two images represent confocal slices taken from the maximum intensity projection of the merge. (C) Images of *clc*$^-$ and *chc*$^-$ cells chemotaxing to a micropipette containing 1 μM cAMP. (D) Confocal fluorescent images of ACA-YFP/*aca*$^-$ and ACA-U-YFP/*clc*$^-$ cells colabeled with lysotracker red. The asterisk represents the position of the micropipette.

in their ability to enrich ACA-YFP at their back and to align in a head-to-tail fashion during chemotaxis (Fig. 3, E and F; Video 4; and Table S1). These findings show that microtubules are essential for ACA-containing vesicles to accumulate at the back of polarized cells and for streaming during chemotaxis.

ACA vesicles are not targeted to lysosomes and require proper assembly of clathrin for trafficking

To gain more insight into the nature of the ACA-labeled vesicles, we first performed colocalization studies with lysosomal markers. Fully differentiated ACA-YFP/*aca*$^-$ cells were incubated with labeled Dextran–Alexa 568 or BSA–Alexa 568 for 1 h, extensively washed, and plated on coverslips, and the YFP and Alexa signals were visualized by confocal microscopy (Hacker et al., 1997). We found no colocalization between ACA vesicles and the endocytosed Dextran–Alexa 568 or BSA–Alexa 568 (Fig. 4 A and not depicted), confirming and extending previous studies using lysotracker (Kriebel et al., 2003). These findings establish that ACA vesicles are not associated with lysosomes.

We then used the impermeable dye FM4-64 to assess the role of endocytic trafficking in the dynamic distribution of ACA. This dye fluoresces only when incorporated in the plasma membrane and, once internalized, it becomes trapped in intracellular vesicles, thereby representing a useful tool to visualize endocytosis (Vida and Emr, 1995). Differentiated ACA-YFP/*aca*$^-$ cells were incubated with FM4-64 under conditions designed to minimize the contractile vacuoles (see Materials and methods) and examined at various time points by confocal microscopy. Under these conditions, FM4-64 labeling becomes restricted to small endosome-like compartments (Zhu and Clarke, 1992; Aguado-Velasco and Bretscher, 1999). As expected, we observe strong plasma membrane labeling 1 min after the addition of FM4-64, which readily internalizes to label intracellular compartments after 30 min (Fig. 4 B). Under these conditions, we consistently see colocalization of the dye with ACA-YFP vesicles in a central perinuclear area (Fig. 4 B). Yet, distinct red (FM4-64) and green (ACA-YFP) vesicles are also present throughout the polarized, migrating cells (Fig. 4 B, Merge and Slice Merge). We also observe portions of the ACA-YFP compartment at the back of cells that does not colocalize with FM4-64, both at the cell

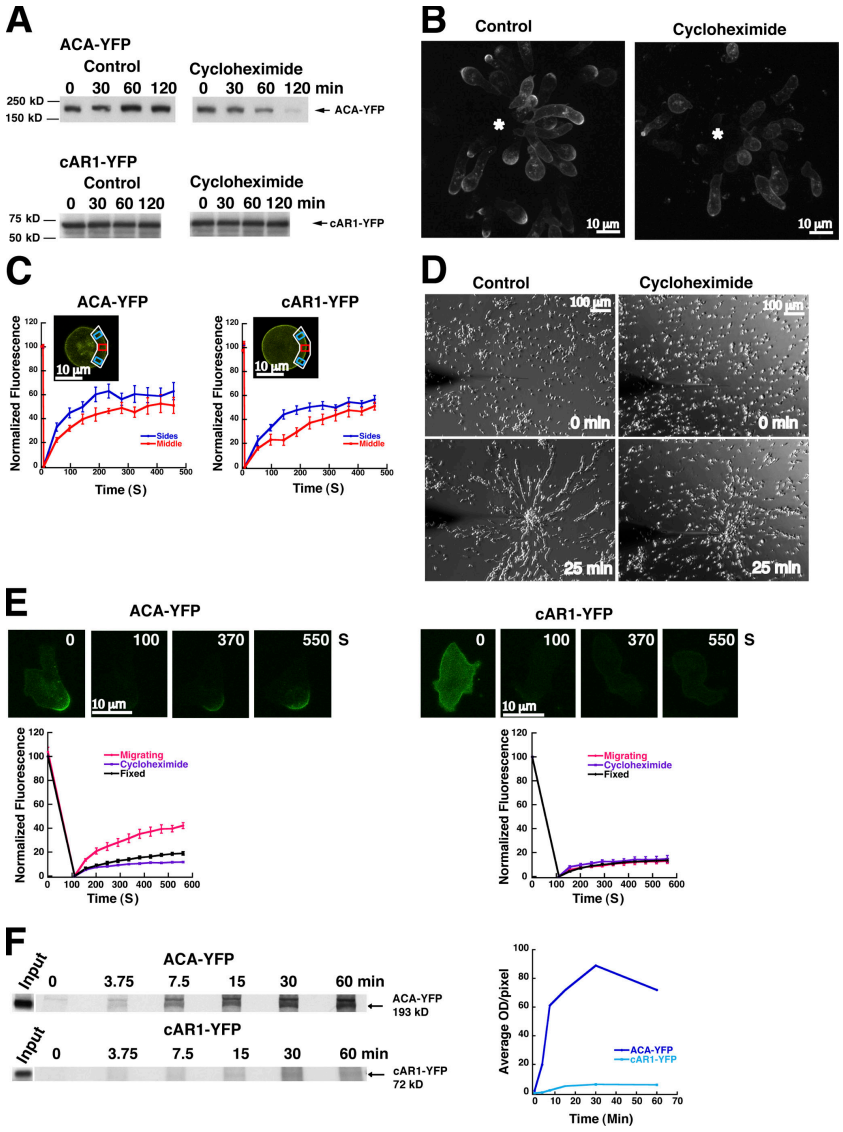

Figure 5. **ACA trafficking requires de novo ACA synthesis.** (A) Western analysis showing the expression of ACA-YFP from ACA-YFP/*aca*⁻ cells or cAR1-YFP from cAR1-YFP/*car1/3*⁻ cells in the presence or absence of 400 µM CHX. Similar findings were observed when we monitored endogenous levels of ACA in WT cells. See Materials and methods for details. Representative data of at least three independent experiments are shown. (B) Fluorescent maximum intensity projections of ACA-YFP/*aca*⁻ cells chemotaxing to a micropipette filled with 1 µM cAMP in the presence or absence of CHX (1-h treatment). The asterisk represents the position of the micropipette. (C, inset) Confocal fluorescent images of ACA-YFP/*aca*⁻ or cAR1-YFP/*car1/3*⁻ cells treated with CHX (1 h) showing the bleached area (white) and the side (blue) and middle (red) boxes where the fluorescence recovery is monitored. The graphs depict the recovery of ACA-YFP and cAR1-YFP. See Fig. 2 B for details. (D) Bright field images of ACA-YFP/*aca*⁻ cells chemotaxing to a micropipette containing 1 µM cAMP in the presence or absence of CHX (1-h treatment). Also see Video 5. Identical results were observed with WT cells. (E, top) Confocal fluorescent images of ACA-YFP/*aca*⁻ or cAR1-YFP/*car1/3*⁻ migrating cells before and after complete bleach. The numbers represent the time (in seconds) after the bleach. Also see Video 6. The graphs depict the total fluorescent recovery of ACA-YFP or cAR1-YFP from the entire cell under various conditions. Data are presented as a mean of five cells ± SEM. It is the short maturation time of YFP that has allowed us to visualize the quick recovery of ACA. Cells expressing ACA-GFP show no recovery after total bleaching (not depicted). (F, right) Radiographs depicting the incorporation of ^{35}S-Translabel into ACA-YFP or cAR1-YFP at various time points after adding it to ACA-YFP/*aca*⁻ and cAR1-YFP/*car1/3*⁻ migrating cells (see Materials and Methods for details). The input lane shows a Western analysis (using an α-GFP antibody) of pulled down ACA-YFP and cAR1-YFP samples and depicts the starting amounts of protein for both ACA-YFP and cAR1-GFP. The graph shows the optical density (OD) values from the radiographs. Representative data of at least three independent experiments are shown. Videos are available at http://www.jcb.org/cgi/content/full/jcb.200808105/DC1.

periphery and as intracellular vesicles. We did however observe colocalization of ACA-YFP and FM4-64 at the back of cells 1 min after the addition of FM4-64. We envision that this colabeling represents accumulated extracellular membrane present at the back of cell (see ACA vesicles are distributed within MVBs that are shed during migration). Together, these findings suggest that endocytic trafficking is not directly involved in the biogenesis of ACA vesicles targeted to the back of migrating cells.

We next turned our attention to cells lacking clathrin. Clathrin is a triskelion made of three clathrin heavy chains (CHCs) and three clathrin light chains (CLCs; Brodsky et al., 2001). *Dictyostelium chc*⁻ cells exhibit classical endocytosis defects (O'Halloran and Anderson, 1992; Ruscetti et al., 1994). In contrast, *clc*⁻ cells show no such defects and have normal triskelion structures, but exhibit less clathrin structures at the membrane and more in the cytosol. These findings suggest that the CLCs are required to optimally assemble clathrin at the plasma membrane (Wang et al., 2003). We found that cells lacking either the CHCs or the CLCs are able to properly develop and to chemotaxe to a point source of chemoattractant, a finding reported by others for *chc*⁻ cells (Wessels et al., 2000; Table S1). Interestingly, both cell lines exhibit significant streaming defects (Fig. 4 C). We attempted to transfect *chc*⁻ and *clc*⁻ cells with the ACA-YFP expression plasmid on several occasions but were not successful in generating stable cell lines. We reasoned that overexpression of a catalytically active ACA might be detrimental to these cells. We therefore used a mutant of ACA that lost the capacity to be activated by G proteins (ACA-U-YFP) but retains a normal cellular distribution pattern (Kriebel et al., 2003). Although we were unable to obtain *chc*⁻ cells expressing ACA-U-YFP, we successfully generated stable ACA-U-YFP/*clc*⁻ cells. We found the distribution of ACA-U-YFP to be aberrant in these cells, with a dramatic loss of plasma membrane staining and loss of enrichment at the back and a significant accumulation of ACA-YFP in large intracellular vesicles that costain with lysotracker (Fig. 4 D) or Dextran–Alexa 568 (not depicted). These large compartments were also readily observed in untransfected *clc*⁻ cells (unpublished data). We conclude that the loss of CLCs leads to the mislocalization of ACA and aberrant streaming. Because we were unable to study ACA distribution

in *chc*$^{-}$ cells, it is impossible to for us to definitively address the role of clathrin-mediated endocytosis in ACA vesicle trafficking. In any case, our findings using *clc*$^{-}$ cells clearly establish that proper clathrin assembly is required for normal cellular distribution of ACA.

ACA trafficking requires de novo ACA synthesis

To assess the role of protein synthesis in the cellular distribution of ACA, we treated ACA-YFP/*aca*$^{-}$ cells with cycloheximide (CHX) and subjected them to FRAP analyses. It has previously been shown that CHX treatment does not alter the ability of *Dictyostelium* cells to sense chemoattractant gradients or to uptake membrane by endocytosis; yet it does inhibit the ability of *Dictyostelium* cells to migrate directionally (Clotworthy and Traynor, 2006). We therefore closely observed the effect of CHX over time. We first monitored the expression level of ACA-YFP using Western analysis and found that it is significantly decreased after CHX treatment (Fig. 5 A). An identical treatment did not alter the expression level of cAR1-YFP (Fig. 5 A). We observed that ACA-YFP cells treated with CHX for 1 h, which shows a mild decrease in ACA-YFP expression, exhibit a significant and specific defect in their ability to enrich ACA-YFP at their back, the expression of ACA-YFP at the front of cells remains unchanged (Fig. 5 B, Table S1, and not depicted). Under these same conditions, the fluorescence recovery of the ACA-YFP signal after photobleaching is also altered and mimics the membrane diffusion pattern of the cAR1-YFP cells, with the side boxes recovering before the middle box (Fig. 5 C). CHX-treated cells were then exposed to a chemoattractant gradient. We find that CHX treatment does not affect the ability of cells to polarize and migrate toward the micropipette, although they consistently move more slowly (Table S1). However, as expected, CHX-treated cells display severe streaming defects (Fig. 5 D and Video 5, similar findings were obtained after a 30-min CHX treatment, available at http://www.jcb.org/cgi/content/full/jcb.200808105/DC1). Together, these findings establish that ACA synthesis is required to maintain its enrichment at the back of cells and for streaming. Although we certainly cannot rule out that the expression of other proteins is also affected by CHX treatment, the fact that we observe dramatic effects on ACA with short-term CHX treatment underscores the importance of ACA synthesis during streaming.

The extent of ACA synthesis was also observed in real time after total bleaching, a process in which the entire cell is bleached. When differentiated and polarized ACA-YFP/*aca*$^{-}$ cells are subjected to such a treatment, the fluorescent signal quickly and significantly recovers (Fig. 5 E and Video 6, available at http://www.jcb.org/cgi/content/full/jcb.200808105/DC1). To assess the contribution of fluorophore photoconversion in this response (Giepmans et al., 2006), we subjected fixed ACA-YFP cells to a total bleach and found that the extent of fluorescence recovery in the live migrating cells far exceeds the innate ability of YFP to spontaneously fluoresce (Fig. 5 E). As expected from our findings, we observed that CHX treatment abolishes the recovery of ACA-YFP and that cAR1-YFP/*car1/3*$^{-}$ cells show no significant fluorescence recovery under all conditions tested (Fig. 5 E).

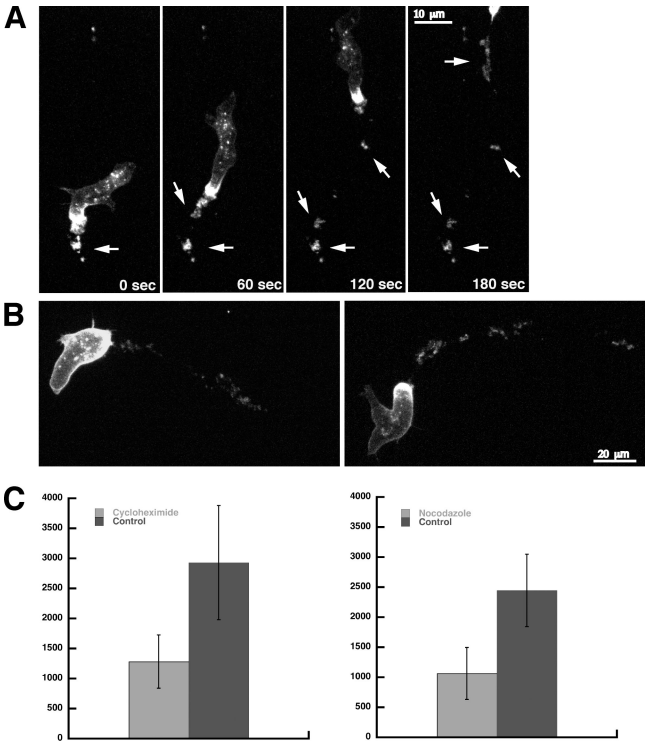

Figure 6. **Migrating cells leave behind ACA-containing vesicles.** (A) Sequential fluorescent maximum intensity projections of an ACA-YFP/*aca*$^{-}$ cell leaving tracks containing ACA-YFP. Arrows indicate tracks. Also see Videos 7 and 8. (B) Fluorescent maximum intensity projections of ACA-YFP/*aca*$^{-}$ cells leaving tracks containing ACA-YFP. (C) Graph depicting the fluorescence intensity of tracks/cell in ACA-YFP/*aca*$^{-}$ cells treated with 60 µM Noco or 200 µM CHX for 1 h and migrating to a micropipette filled with 10 µM cAMP (see Materials and Methods and Fig. S3 for details). Data represent means ± SEM of four independent experiments totaling ~165 cells. Online supplemental material is available at http://www.jcb.org/cgi/content/full/jcb.200808105/DC1.

We performed [^{35}S]methionine/cysteine labeling experiments to gain insight into the rate of ACA de novo synthesis. We added [^{35}S]methionine/cysteine to fully differentiated ACA-YFP cells and at specific time points assessed the ^{35}S content in ACA immunoprecipitates. We measured [^{35}S]methionine/cysteine incorporation in a specific band of 170 kD (Fig. 5 F), which comigrates with pulled down ACA-YFP and is missing in wild-type (WT) cells (not depicted). Under these conditions, incorporation of [^{35}S]methionine/cysteine in ACA-YFP is rapid and robust. It is detected at the earliest time point collected (3.75 min) and peaks at 30–60 min. In contrast, cAR1-YFP cells show trace levels of [^{35}S]methionine/cysteine incorporation (Fig. 5 F) in spite of a higher methionine and cysteine content, compared with ACA-YFP.

ACA vesicles are distributed within multivesicular bodies (MVBs) that are shed during migration

Upon closer examination of ACA-YFP/*aca*$^{-}$, we found that actively migrating cells leave behind membranous structures rich in ACA (Fig. 6, A and B; and Videos 7 and 8, available at http://www.jcb.org/cgi/content/full/jcb.200808105/DC1). Uchida and Yumura (1999) originally coined the term "cellular tracks"

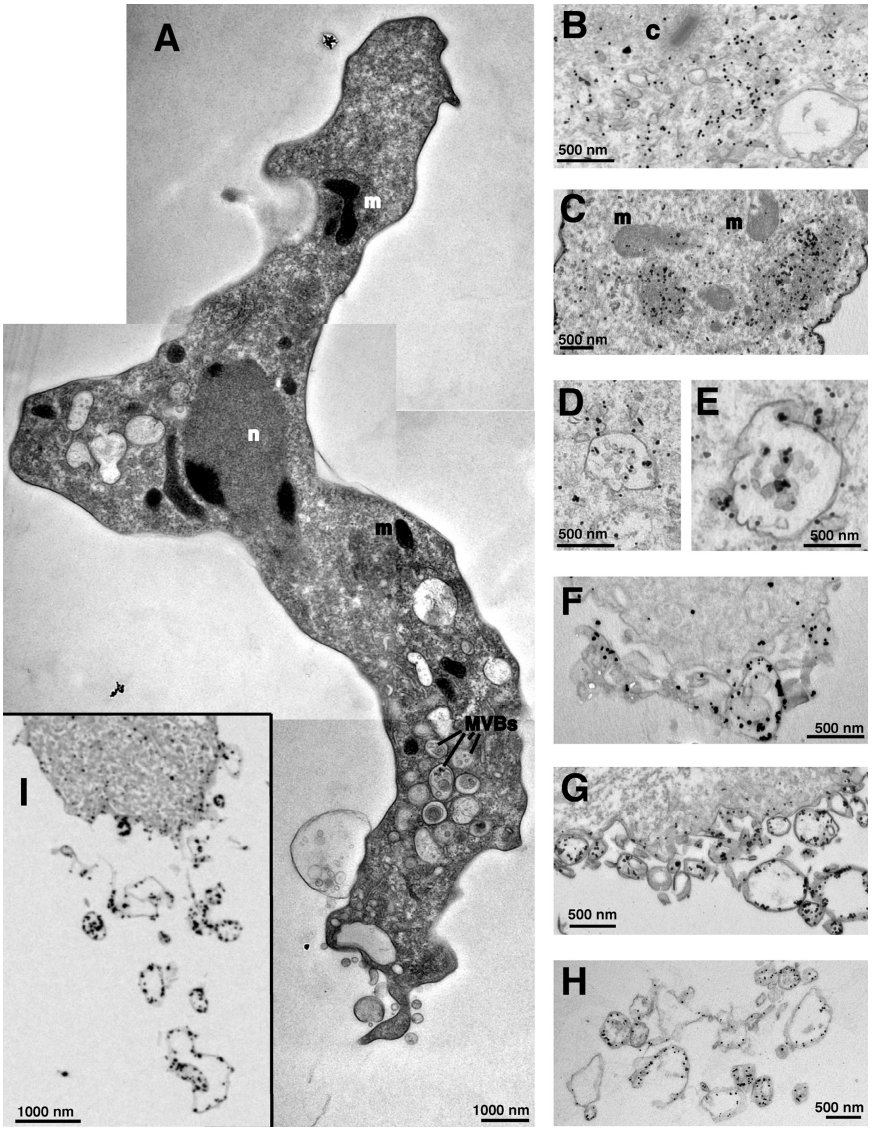

Figure 7. **Ultrastructural analysis of the distribution of ACA in migrating cells.** (A) Mosaic of hyperbaric freeze EM images displaying an entire migrating ACA-YFP/*aca*$^-$ cell. (B–I) Immunogold EM images depicting the distribution of ACA-YFP in various cellular compartments. m, mitochondria; n, nucleus; c, centriole; PM, plasma membrane. See text for details.

when they observed that *Dictyostelium* cells leave tracks fluorescently labeled with concavalin A. They observed that chemotaxis-competent cells often migrate on these tracks and proposed that they help cells migrate directionally. To gain more insight into this, we measured the amount of ACA-containing tracks in WT and Noco- or CHX-treated cells. As both treatments hamper the asymmetrical delivery of ACA at the back of cells and the ability of cells to stream, we reason that they would also lead to the generation of fewer tracks. We monitored >160 actively migrating cells for each condition and find that either treatment significantly reduces the amount of ACA-positive trails by >50% compared with control (Fig. 6 C and see Fig. S3 for details). The expression level of ACA-YFP in control and Noco- or CHX-treated cells was identical as monitored by Western and FACS analyses (unpublished data). Together, these findings suggest that the ACA-containing tracks act as directional cues during chemotaxis.

We used hyperbaric freeze EM to obtain high quality ultrastructural information on the back of polarized migrating cells and on the nature of the extracellular, ACA-positive structures proximal to it. Fig. 7 A depicts a typical cell with a clearly polarized ultrastructure, a centrally located nucleus, and various types of vesicles concentrated toward one end of the cell, which we presume is the back. We used immunogold EM to visualize the distribution of ACA. As presented in Fig. 7 (B–I), we found gold labeling to be particularly dense at the plasma membrane and in extracellular as well as intracellular vesicles. Quantification of gold particles revealed a sevenfold enrichment at the plasma membrane relative to the nuclear membrane (4.1 ± 0.38 vs. 0.73 ± 0.13 gold particles/μm, respectively). Intracellularly, the gold labeling was particularly dense in three specific locations: on highly tubular, membranous structures that cluster around the centriole (Fig. 7 B), on densely packed structures (Fig. 7 C), and on MVBs (Fig. 7, D and E). Although, we do not know the exact nature of the highly tubular structures, we envision that they are part of the biosynthetic pathway that feeds into the vesicular pool of ACA. The extent of MVBs labeling was striking as it occurred on 24% of identified MVBs. We did not observe labeling of lysosomal compartments, which confirmed our colocalization studies with ACA-YFP

and Dextran–Alexa 568 (Fig. 4 A). Remarkably, we observed labeling on an extensive network of extracellular vesicles both at the back of cells, proximal to the plasma membrane (Fig. 7, F and G), and as trails (Fig. 7, H and I), presumably corresponding to the ACA-positive trails we observe in our live imaging of migrating ACA-YFP cells (Fig. 6 and Videos 7 and 8). Interestingly, we also routinely observed FM4-64 labeling at the back of cells that colocalized with ACA-YFP (Fig. 4 B). As this occurred very early after FM4-64 addition, we reason that the FM4-64 is actually labeling accumulated extracellular membrane present at the back of cells. Together, these findings establish that ACA is present at the plasma membrane and on complex intracellular vesicles, which appear to be specifically released at the back of cells.

Discussion

Our findings show that vesicle trafficking is required for the asymmetrical distribution of ACA in polarized *Dictyostelium* cells. We show that the distribution of ACA at the back of cells results from an accumulation of vesicles that mainly arise from a biosynthetic pathway and that intact microtubule and actin networks are required to maintain this enrichment. Interestingly, EM analyses reveal that ACA is found on MVBs that accumulate at the back of cells where they are poised to release their contents as exosomes and propagate chemotactic signals. Although we do not know the exact mechanism by which ACA is trafficked to MVBs, our findings clearly bring forward a pathway that is distinct from the canonical pathway where sorting into MVBs destines proteins to lysosomal degradation. We observed no colocalization of ACA vesicles with lysotracker. Furthermore, FM4-64 colabeling with ACA vesicles is restricted to a pool of perinuclear vesicles, and large portions of the ACA-enriched compartment at the back of cells are devoid of FM4-64, suggesting that endocytosis plays, at best, an indirect role in the biogenesis of ACA-labeled vesicles targeted to the back of migrating cells. Rather, the observation that the enrichment of ACA at the back of cells is abrogated with CHX treatment implies that this ACA compartment involves a biosynthetic pathway. Intriguingly, we also found that clathrin assembly is essential for proper ACA localization and streaming. Studies in *Dictyostelium* have established that, in addition to regulating endocytosis, clathrin controls cytokinesis, osmoregulation, lysosome trafficking, and cell polarity (Niswonger and O'Halloran, 1997; Wessels et al., 2000; Gerald et al., 2001). Moreover, it has been shown that a significant amount of CHC is transiently concentrated at the back of migrating cells (Damer and O'Halloran, 2000). It remains to be determined if this specific pool of clathrin colocalizes with or regulates ACA.

Our studies show that migrating cells secrete vesicles that are rich in ACA, generating extensive extracellular tracks. We propose that the spatial enrichment of ACA vesicles at the back of cells and their subsequent release in the form of tracks are important components of the streaming process, where cells align in a head-to-tail fashion during chemotaxis. Remarkably, our EM analyses show that the gold particles specifically label the cytosolic face of the vesicles, both inside and outside the cell. As the YFP is linked to the C-terminal, cytosolic side of ACA, where the catalytic loops reside, these findings suggest that the cells are releasing vesicles that contain cAMP. We propose that the vesicles are secreted as exosomes, where vesicles are released by the fusion of the MVBs external membrane with the plasma membrane (Thery et al., 2002). We do not know how cAMP is released from the vesicles. The vesicles possibly express a pump that actively releases the cAMP, a process that could be regulated. Alternatively, the vesicles may just burst in response to osmotic pressure, thereby releasing their content nonspecifically. In any case, this vesicular transport of cAMP provides an attractive mechanism for sustained chemoattractant release. Indeed, when exposed to a chemoattractant, many cells respond by making more chemoattractant, thereby amplifying the original signal. Yet, as most chemoattractants are small, highly diffusible molecules, the extent by which they can persist and reach neighboring cells has presented a challenge. The packaging of chemoattractants within secreted vesicles could allow the signal to persist and reach long distances.

We show that the chemoattractant-mediated activation of ACA in LatA-treated cells, which are devoid of ACA-containing vesicles, is dramatically inhibited compared with untreated cells. It has been proposed that polymerized actin amplifies phosphatidylinositol-3-kinase (PI3K) activity after chemoattractant stimulation (Weiner et al., 2002; Sasaki et al., 2004). As ACA activity is PI3K-dependent, this raises the possibility that the effect of LatA on ACA activity could be mediated through reduced PI3K activity. However, we find significant phosphatidylinositol (3,4,5)-trisphosphate generation in LatA-treated cells (Parent et al., 1998; this study). We therefore conclude that the strong inhibition of ACA activity in LatA-treated cells is not related to effects on PI3K. Indeed, we have previously shown that PI3K activity regulates ACA activation, but not its cellular distribution (Comer and Parent, 2006). Rather, our findings suggest that the activatable pool of ACA is restricted to the vesicular pool of the enzyme. Interestingly, we reported that a constitutively active mutant of ACA is aberrantly distributed in cells, showing a dramatically reduced enrichment of ACA at the back of cells and a higher number of internal vesicles, ultimately giving rise to streaming defects when expressed in *aca*$^{-}$ cells (Kriebel et al., 2003). These findings suggest that there is a relationship between the cellular distribution of ACA and its catalytic activity. It has previously been shown that the highest peak of *Dictyostelium* ACA activity resides in a sedimentable light membrane fraction mainly composed of small vesicles (Hintermann and Parish, 1979). In addition, Maeda and Gerisch (1977) have shown that intracellular vesicles and vacuoles change in numbers in response to cAMP pulses and extensively fuse with the plasma membrane. This led them to propose that exocytosis is responsible for the secretion of cAMP in *Dictyostelium*. However, Dinauer et al. (1980) showed that cAMP is immediately secreted after its synthesis and proposed that cAMP is not stored in vesicles. Our findings clearly show the existence of an asymmetrically distributed vesicular pool of ACA in polarized cells that is responsible for the alignment of cells into streams, presumably through the release of cAMP at the back of the cell. Whether or not cAMP is stored in vesicles for release

at a later time or is synthesized in vesicles and then immediately released cannot be discerned by our data. However, our results are compatible with both options.

Microtubule cortical capture plays a key role in controlling vesicle trafficking, although the underlying mechanistic basis for this is not yet defined (Gundersen et al., 2004). In this context, the actin-based motor myosin V has been shown to be involved in mediating the movement of cargo from microtubules to actin filaments at the cell cortex (Wu et al., 2006). We studied *Dictyostelium* cells lacking myosin J (MyoJ), which shares homology with class V and IX myosins (Hammer and Jung, 1996; Peterson et al., 1996). Cells lacking MyoJ showed significant streaming defects and mislocalization of ACA after 5 h of development. However, these defects were completely reversible by 7 h of development (unpublished data), suggesting that the MyoJ-null cells exhibit a developmental delay or that redundant components expressed later can foster the delivery of ACA vesicles to the back of cells. We also find that polarized *Dictyostelium* cells have an extensive microtubule network at their back, which originates from a MTOC that is positioned behind the nucleus. Remarkably, the leading edge of these cells is virtually devoid of microtubule fibers. We envision that this architecture, which is also observed in neutrophils and migrating lymphocytes, is present to preferentially accommodate cargo delivery to the back of cells (Ratner et al., 1997; Eddy et al., 2002). In contrast, in slow moving fibroblasts, the MTOC is positioned in front of the nucleus and microtubules primarily extend to the front of these cells during scratch wounding–mediated migration (Kupfer et al., 1982; Gundersen and Bulinski, 1988). We predict that this fundamental difference between cell types underlies distinct requirements for cargo delivery to the front and back of cells in amoeboid (*Dictyostelium*, neutrophils, and lymphocytes) versus mesenchymal (fibroblasts) migration. Interestingly, as previously observed in neutrophils, we found that a fully functional microtubule network is not required for chemotactic migration in *Dictyostelium* cells (Niggli, 2003; Xu et al., 2005). In neutrophils, it does, however, enhance the activity of Rho kinase, which is involved in controlling actomyosin-dependent back contractility. It therefore appears that in both *Dictyostelium* and neutrophils, microtubules regulate "backness" events.

Our findings have general implications for chemoattractant delivery and group migration. Secreted vesicles could act as tracks, allowing cells to follow a path left by a leading cell. Many cells have been shown to secrete vesicular components, including exosomes. For instance, B cells and dendritic cells secrete exosomes that carry major histocompatibility complex class I and II (Raposo et al., 1996; Zitvogel et al., 1998). Activated platelets secrete exosomes by fusion of α-granules and endothelial cells release TNFR1 from exosome-like vesicles to modulate TNF bioactivity (Heijnen et al., 1999; Hawari et al., 2004). Interestingly, it has recently been shown that T cells store the chemokine RANTES in small vesicles that are distinct from lysosomal secretory granules and release it after T cell receptor stimulation (Catalfamo et al., 2004); this situation is analogous to what we report here. Finally, vesicle shedding has been observed in a wide variety of tumor cells (Dolo et al., 1998; Taverna et al., 2003). In particular, invasive melanoma cells release cell fragments in a migration-dependent manner, and the tracks left behind have been proposed to represent zones of facilitated invasion of neighboring cells, allowing the migration of cells in chains or streaming (Mayer et al., 2004). In this context, it will be interesting to determine if the release of chemoattractant in vesicles also plays a role in the paracrine loop regulating the comigration of macrophages and carcinoma cells during metastasis (Yamaguchi et al., 2005). The findings reported here suggest that this fascinating mode of cell–cell communication appeared early during evolution.

Materials and methods

Materials

The GFP–α-tubulin constructs were provided by A. Muller-Taubenberger (Ludwig Maximilians University Munich, Munich, Germany) and G. Gerisch (Max Planck Institute of Biochemistry, Martinsried, Germany). T. Jin (National Institute of Allergy and Infectious Diseases, National Institutes of Health, Rockville, MD) provided the cAR1-YFP construct, R. Graf (University of Potsdam, Postdam-Golm, Germany) provided the γ-tubulin antibody, J. Hammer (National Heart, Lung, and Blood Institute, National Institutes of Health, Bethesda, MD) provided the *myoIb/c*$^{-/-}$ and *myoJ*$^{-}$ cells, and T. O'Halloran (University of Texas at Austin, Austin, TX) provided the *clc*$^{-}$ and *chc*$^{-}$ cells. The α-tubulin antibody, developed by J. Frankel and E.M. Nelsen, was obtained form the Developmental Studies Hybridoma Bank developed under the auspices of the National Institute of Child Health and Human Development and maintained by the University of Iowa.

Cell culture and differentiation

WT (AX_3), ACA-YFP/*aca*$^{-}$, and cAR1-YFP/*car1/3*$^{-}$ cells were grown in shaking cultures to ∼4 × 10^6 cells/ml in HL5 media (Kriebel et al., 2003). They were harvested by centrifugation, washed once in developmental buffer (DB; 5 mM Na_2HPO_4, 5 mM NaH_2PO_4, pH 6.2, 2 mM $MgSO_4$, and 200 μM $CaCl_2$), and finally resuspended in DB at 2 × 10^7 cells/ml. To allow differentiation, the cells were shaken at 100 rpm for 4–7 h with repeated pulses of 75 nM cAMP (Devreotes et al., 1987; Parent and Devreotes, 1996a). The cells were then processed according to the assay performed.

Confocal fluorescence microscopy

Cell preparation. Cells were differentiated as described in the previous paragraph. A 200-μl sample of cells was removed, centrifuged, resuspended in 200 μl of phosphate buffer (PB; 5 mM Na_2HPO_4 and 5 mM NaH_2PO_4, pH 6.2), diluted 1:10 in PB, spotted on 2-well chamber slides (Laboratory-Tek; Thermo Fisher Scientific), and allowed to adhere for 5 min before adding 1 ml PB to fill the chamber.

Confocal microscopy detailing ACA-YFP distribution in cells. ACA-YFP/*aca*$^{-}$ cells were prepared for microscopy and observed with a microscope (Axiovert 200; Carl Zeiss, Inc.) equipped with a confocal system (Ultraview ERS; PerkinElmer) with a spinning disk head (Yokogawa) and a camera (Orca ER; Hamamatsu). Single plane images and z stacks were taken using 63 and 100× plan neofluor objectives (Carl Zeiss, Inc.) and z stacks were arranged in maximum intensity projections.

Confocal microscopy with dextran-Alexa and lysotracker. Cells were incubated with 10 mM dextran–Alexa 568 at 10,000 MW (Invitrogen) for 1 h or with 4 μM lysotracker red DND 99 (Invitrogen) for 30 min. The cells were washed and plated on chambered slides. Confocal images were taken with a microscope (510 LSCM; Carl Zeiss, Inc.) using a 63× plan neofluor objective.

Confocal microscopy with FM4-64. Cells were pretreated with 0.1 M sorbitol in PB before the addition of FM4-64 to reduce the formation of contractile vacuoles, a specialized organelle designed to expel water from *Dictyostelium* cells that is extensively labeled with FM4-64. 2 μM FM4-64 was added to cells for 30 min. Both 0.1 M sorbitol and FM4-64 were present with the cells while imaging. Z stacks encompassing the entire cells were taken using the confocal system equipped with a spinning disk head and a camera. FM4-64 and ACA-YFP were visualized in red and green channels, respectively.

FRAP

Vegetative, 5-h differentiated nonpolar, 5-h differentiated polar nonmigrating, and polar-migrating ACA-YFP/*aca*$^-$ or cAR1-YFP/*car1/3*$^-$ cells were spotted onto chamber slides and allowed to adhere for 5 min. 5-h differentiated nonpolar cells were obtained by diluting (1:100–1:500) pulsed cells before spotting them on a chamber slide as previously described (Kriebel et al., 2003). Polar, nonmigrating cells were obtained by allowing the diluted cells to slowly polarize on the chamber slide. This occurs secondary to the buildup of cAMP, which is spontaneously released. Polar-migrating cells were obtained by spotting 5-h differentiated cells 10-fold more concentrated. To visualize the entire cell on the microscope, cells were flattened with a 4-mm thick slice of agarose gel so that the entire cell body was within a height that could be visualized and bleached by a wide-open pinhole of ~5 µM. The bleach box was expanded to include a portion of the top and the bottom membrane to minimize the contribution of diffusion from above and below the bleach box. A section of the cell periphery in zoom 3 was exposed to two iterations of saturating 488-nm laser light inducing a partial bleach. A series of single plane (5 µm) time-lapse images were taken using a 63× plan neofluor objective. The microscope's pinhole was opened as wide as possible (5 µm) so that the images depicted the status of the entire cell's periphery from top to bottom before, during, and after bleaching. From these images, fluorescent intensity was measured in three regions of interests (ROIs). Two ROIs included areas on either side of the bleached membrane, just inside the bleached area. One ROI encompassed a middle portion of the bleached cell periphery. Starting fluorescence intensity for each ROI was calculated by averaging two images taken 5 s apart before the bleach. A single image taken just after the bleach was used to determine the bleach level. Each subsequent image was taken every 45 s after bleaching and used to determine the recovery of fluorescence over time. All image processing was done using the LSM 5.0 software (Carl Zeiss, Inc.). The fluorescent intensity values of each ROI over time was normalized so that the starting value was 100% and the value after bleaching was 0%. The normalized fluorescent intensity values of all ROIs were obtained from five independent cells, averaged and plotted over time. FRAP was measured in migrating cells using the same conditions. However, we only monitored the fluorescence recovery at a single ROI located at the center of the bleached box. The side bleach ROIs were left out because the dynamic nature of the cell periphery in migrating cells made the location of these areas difficult to discern from frame to frame. However, the center area was easily identifiable because it was always at the apex of the curve of the plasma membrane at the back of the cell. This center ROI was redrawn on the corresponding position of each image as the cell moved. The data were processed as described. FRAP with complete bleaching was achieved by performing three bleaches of four iterations of saturating 488-nm wavelength, 45 s apart. Only one ROI was used to monitor fluorescence and it encompassed the entire cell. Fluorescent intensity values were obtained, normalized, averaged, and graphed as described.

FRAP with cytoskeletal disruption and protein synthesis inhibitors. 5 µM LatA (for 45–60 min; Invitrogen), 30–60 µM Noco (for 60 min; EMD), or 200–400 µM CHX (for 60 min; Sigma-Aldrich) was added to cells spotted on a chamber slide. Gel slabs soaked in double the designated concentration of drug for 2 h were carefully layered on top of the treated cells. FRAP analyses were performed as described.

Deconvolution microscopy

ACA-YFP/*aca*$^-$ cells were differentiated, plated, and allowed to polarize as described. They were quickly fixed at room temperature for 10 min in 1% formaldehyde, 0.1% glutaraldehyde, and 0.01% Triton X-100 in 15 mM Pipes/1 mM EGTA. After blocking in 10% FBS in PBS, the cells were incubated with an anti–α-tubulin antibody (1:200; Developmental Studies Hybridoma Bank) followed by an anti–mouse IgG1 antibody conjugated to Alexa 568 (Invitrogen). YFP and Alexa 568 images were taken with a DeltaVision system (Applied Precision, LLC) using a 63× objective. Deconvolution was performed with DeltaVision software and 3D reconstructions were made with Imaris software (Bitplane AG). The quantification studies were done with the same fixative and staining protocol. Cells were scored for location of the MTOC with respect to the nucleus (stained with DAPI) and the presence of microtubules going to the leading edge of the cell.

Quantification of the cell track fluorescence

Starved and pulsed cells were plated on 3-mm plates in 1 ml PB in the presence of 200 µM CHX or 60 µM Noco (or appropriate control solvent) at room temp for 1 h. Cells were harvested using a cell scraper, pelleted and resuspended in 500 µl PB containing the appropriate drug conditions, spotted on chamber slides, allowed to attach, and covered with 1.5 ml PB containing the appropriate drug or control. The cells were allowed to migrate toward a micropipette filled with 10 µM cAMP for ~20 min. A 1-µm confocal slice focused on the tracks at the bottom of the chamber was taken every 10 s using a microscope with a 488-nm laser and a 63× plan neofluor objective. These images were taken in conjunction with differential interference contrast images. Track fluorescence was obtained using iVision-Mac version 4.0.10 software (BioVision Technologies). Background fluorescence values were taken from starting images and subtracted from all images in a series. Segments were drawn around fluorescent debris in the initial image and transferred to the final image of the series (see Fig. S3 for details). New segments were drawn on the final image of the series around fluorescent tracks excluding debris denoted by segments from the initial image. Cell track fluorescence was determined by measuring the fluorescence in segments around tracks. Cells were counted manually as they entered the field of view. Fluorescent 1-µm confocal images and corresponding differential interference contrast images were merged using the color join command in iVision to create images of cells in Fig. S3. Fluorescent intensity in segments marking debris was set to 0 debris in the merged images to emphasize only the tracks left behind by migrating cells (Fig. S3).

Chemotaxis assay

The chemotaxis assays were performed as previously described (Kriebel et al., 2003). In brief, 5–7-h differentiated cells were plated on chambered cover slides as described previously (Kriebel et al., 2003). Chemoattractant gradients were generated using a microinjector (Eppendorf) using micropipettes filled with 1 µM cAMP. The micropipette was placed into chambered cover slides and images were captured at specified times.

ACA activity and cytosolic regulator of ACA (CRAC) translocation assays

ACA and CRAC translocation assays were performed as previously described (Kriebel et al., 2003; Comer et al., 2005).

^{35}S metabolic labeling

5-h developed cells were placed directly into 35-mm Petri dishes (10×10^6 cells/dish). After the cells had adhered for 5 min, 420 µCi of TRAN^{35}S-Label (MP Biomedicals) was added to each plate. One plate was harvested for each designated time point, the cells were spun, resuspended in IP buffer (40 mM Tris-HCl, ph 8.0, 2 mM EDTA, 50 mM NaCl, and 1% CHAPS) and Complete protease inhibitor cocktail (Roche), and solubilized for 1 h on ice. After solubilization, 100 µl of a 50/50 protein A sepharose CL-4B (GE Healthcare)/IP buffer slurry was added to each sample and incubated using a rotator for 1 h at 4–8°C to preclear the lysate. The protein A sepharose was removed by centrifugation and 7 µl of anti-GFP rabbit polyclonal (BD) was added per milliliter of lysate and incubated on a rotator overnight at 4–8°C. 100 µl of a 50/50 protein A sepharose slurry was added and incubated for 2 h at 4–8°C to precipitate ACA-YFP or cAR1-YFP. Samples were washed four times with 1 ml IP buffer. The precipitated proteins were released from sepharose beads by adding Laemmli buffer and boiling for 10 min (Laemmli, 1970). The resulting samples were run using the Criterion gel system (Bio-Rad Laboratories) using a 4–20% Tris-HCl gel; the gel was dried and the bands were visualized with Biomax MR film (Kodak).

Immunoblotting

CHX was added to 5-h differentiated cells in shaking flasks containing 2×10^7 cells/ml and pulsed for an additional 2 h. 2.7×10^6 cells were harvested at 0, 30, 60, and 120 min and resuspended in Laemmli buffer (Laemmli, 1970). Whole cell lysates were subjected to a 4–20% Tris-HCl SDS-PAGE analysis using the Criterion gel system and transferred to Immobilon-P (Millipore). The Immobilon-P was blotted with anti-GFP monoclonal antibody (1:5,000; Babco) and detection was performed by chemiluminescence using a donkey anti-mouse horseradish peroxidase–coupled antibody (1:5,000; GE Healthcare) and the ECL Western blotting detection reagents (GE Healthcare).

EM

For immunogold EM staining, cells were differentiated and prepared for microscopy as described. Samples were immunostained for EM using a modification of the method used in Polishchuk et al. (2000). Cells were fixed at room temperature for 15 min in 1% formaldehyde, 0.1% glutaraldehyde, and 0.01% digitonin in 15 mM Pipes/1 mM EGTA, followed

by 15 min in 1% formaldehyde. After blocking in 50 mM NH_4Cl, 0.1% digitonin, and 1% BSA in PBS, the cells were incubated with an anti-GFP antibody (1:500; Abcam) in block solution overnight at 4°C followed by anti-rabbit Fab fragments conjugated to Nanogold particles (1.4-nm particle; Nanoprobes). Staining was enhanced for 7 min with Gold-Enhance (Nanoprobes) made with one part component A, one part component B, one part component C, and three parts PBS. Afterward, the samples were stained with osmium and embedded in epon. Images were taken with a transmission microscope (H-7000; Hitachi High Technologies America, Inc.).

Hyperbaric freeze EM

Differentiated cells were spotted on 50-µm-thick sapphire discs (3 mm in diameter; BAL-TEC) and allowed to adhere. The cells were fixed with 2% formaldehyde and 2% glutaraldehyde in PB for 15 min (just before they started to stream). After three rinses in PB, the discs were dipped into either 5% Ficoll (MW: 70,000) or 10% FCS in PB and sandwiched between two flat aluminum specimen carriers with a Chien slot grid (Ted Pella) as a spacer for high pressure freezing (Reipert et al., 2004). The samples were frozen in a high-pressure freezer (HPM10; BAL-TEC) at a pressure of ~2,000 bar. The frozen samples were transferred to an AFS freeze-substitution system (Leica) and subjected to freeze substitution in 1.0% osmium tetroxide in acetone at –90°C for 3 d and then slowly warmed up (5°C per hour) to 20°C. After several rinses in acetone, the samples were infiltrated with mixtures of epon-aradite (Ted Pella) resin and acetone as follows: 1:2 for 2 h, 1:1 for 4 h, 2:1 overnight, and in pure resin for 24 h with two changes. Finally, the discs were placed into the flat-bottomed BEEM capsules for polymerization at 60°C for 1 d. After polymerization, the sapphire discs were separated from the resin blocks with the aid of liquid nitrogen vapor. Ultra thin sections (~80 nm) were cut on Reichert Ultracut E Microtome (American Optical) and collected on copper slot grids. Sections were counter-stained with uranyl acetate and lead citrate and examined under a transmission electron microscope (CM120; FEI; equipped with an image filter [GIF100; Gatan]) operating at 120 keV. Images were acquired using a cooled charge coupled device camera (Gatan).

Online supplemental material

Fig. S1 shows that ACA activity is inhibited in LatA-treated cells. Fig. S2 shows that CRAC translocation is normal in LatA-treated cells. Fig. S3 shows a mosaic of images displaying the steps used to measure the cell tracks fluorescence. Table S1 is a quantification of streaming parameters during chemotaxis. Video 1 shows maximum intensity projections of differentiated ACA-YFP/*aca*$^-$ cells randomly moving or subjected to a micropipette filled with 1 µM cAMP. Video 2 shows a 3D reconstruction of confocal sections of differentiated ACA-YFP/*aca*$^-$ cells. Video 3 shows a 3D reconstruction of deconvoluted ACA-YFP/*aca*$^-$ cells fixed and stained with an α-tubulin antibody. Video 4 shows differentiated ACA-YFP/*aca*$^-$ cells migrating to a micropipette filled with 1 µM cAMP in the absence or presence of 60 µM Noco. Video 5 shows differentiated ACA-YFP/*aca*$^-$ cells migrating to a micropipette filled with 1 µM cAMP in the presence of 400 µM CHX. Video 6 shows migrating differentiated ACA-YFP/*aca*$^-$ cells just before and after a complete cell bleach. Video 7 shows differentiated ACA-YFP/*aca*$^-$ cells leaving tracks of ACA-YFP visualized using reflection interference microscopy. Video 8 shows maximum intensity projections of migrating differentiated ACA-YFP/*aca*$^-$ cells leaving tracks containing ACA-YFP. Online supplemental material is available at http://www.jcb.org/cgi/content/full/jcb.200808105/DC1.

We thank Drs. Günther Gerisch, Ralph Graf, John Hammer, Tian Jin, Annette Muller-Taubenberger, and Terry O'Halloran for providing materials for this study. We thank Dr. Roberto Weigert for his expertise in EM and generous help; Drs. John Hammer, Julie Donaldson, and Richard Leapman for helpful discussion; Dr. Kunio Nagashima at the Electron Microscopy Laboratory at National Cancer Institute (NCI), Frederick Cancer Research and Development Center, for processing the EM samples; and Dr. Jim McNally for use of his deconvolution microscope at the Fluorescence Imaging Facility at NCI. We would also like to thank the Parent laboratory members for excellent discussions and suggestions and Drs. Anna Bagorda and Paul Randazzo for carefully reading the manuscript. A special thanks goes to Dr. Pierre Coulombe for valuable input.

This research was supported by the Intramural Research Program of the Center for Cancer Research, NCI, National Institutes of Health.

Submitted: 20 August 2008
Accepted: 31 October 2008

References

Affolter, M., and C.J. Weijer. 2005. Signaling to cytoskeletal dynamics during chemotaxis. *Dev. Cell.* 9:19–34.

Aguado-Velasco, C., and M.S. Bretscher. 1999. Circulation of the plasma membrane in *Dictyostelium. Mol. Biol. Cell.* 10:4419–4427.

Bagorda, A., V.A. Mihaylov, and C.A. Parent. 2006. Chemotaxis: moving forward and holding on to the past. *Thromb. Haemost.* 95:12–21.

Brodsky, F.M., C.Y. Chen, C. Knuehl, M.C. Towler, and D.E. Wakeham. 2001. Biological basket weaving: formation and function of clathrin-coated vesicles. *Annu. Rev. Cell Dev. Biol.* 17:517–568.

Catalfamo, M., T. Karpova, J. McNally, S.V. Costes, S.J. Lockett, E. Bos, P.J. Peters, and P.A. Henkart. 2004. Human CD8+ T cells store RANTES in a unique secretory compartment and release it rapidly after TcR stimulation. *Immunity.* 20:219–230.

Clotworthy, M., and D. Traynor. 2006. On the effects of cycloheximide on cell motility and polarisation in *Dictyostelium discoideum. BMC Cell Biol.* 7:5.

Comer, F.I., and C.A. Parent. 2006. Phosphoinositide 3-kinase activity controls the chemoattractant-mediated activation and adaptation of adenylyl cyclase. *Mol. Biol. Cell.* 17:357–366.

Comer, F.I., C.K. Lippincott, J.J. Masbad, and C.A. Parent. 2005. The PI3K-mediated activation of CRAC independently regulates adenylyl cyclase activation and chemotaxis. *Curr. Biol.* 15:134–139.

Damer, C.K., and T.J. O'Halloran. 2000. Spatially regulated recruitment of clathrin to the plasma membrane during capping and cell translocation. *Mol. Biol. Cell.* 11:2151–2159.

Devreotes, P., D. Fontana, P. Klein, J. Sherring, and A. Theibert. 1987. Transmembrane signaling in *Dictyostelium. Methods Cell Biol.* 28:299–331.

Dinauer, M.C., S.A. MacKay, and P.N. Devreotes. 1980. Cyclic 3′,5′-AMP relay in *Dictyostelium discoideum* III. The relationship of cAMP synthesis and secretion during the cAMP signaling response. *J. Cell Biol.* 86:537–544.

Dolo, V., A. Ginestra, D. Cassara, S. Violini, G. Lucania, M.R. Torrisi, H. Nagase, S. Canevari, A. Pavan, and M.L. Vittorelli. 1998. Selective localization of matrix metalloproteinase 9, beta1 integrins, and human lymphocyte antigen class I molecules on membrane vesicles shed by 8701-BC breast carcinoma cells. *Cancer Res.* 58:4468–4474.

Eddy, R.J., L.M. Pierini, and F.R. Maxfield. 2002. Microtubule asymmetry during neutrophil polarization and migration. *Mol. Biol. Cell.* 13:4470–4483.

Franca-Koh, J., Y. Kamimura, and P. Devreotes. 2006. Navigating signaling networks: chemotaxis in *Dictyostelium discoideum. Curr. Opin. Genet. Dev.* 16:333–338.

Franke, J., and R.H. Kessin. 1992. The cyclic nucleotide phosphodiesterases of *Dictyostelium discoideum*: molecular genetics and biochemistry. *Cell. Signal.* 4:471–478.

Gerald, N.J., C.K. Damer, T.J. O'Halloran, and A. De Lozanne. 2001. Cytokinesis failure in clathrin-minus cells is caused by cleavage furrow instability. *Cell Motil. Cytoskeleton.* 48:213–223.

Giepmans, B.N., S.R. Adams, M.H. Ellisman, and R.Y. Tsien. 2006. The fluorescent toolbox for assessing protein location and function. *Science.* 312:217–224.

Gundersen, G.G., and J.C. Bulinski. 1988. Selective stabilization of microtubules oriented toward the direction of cell migration. *Proc. Natl. Acad. Sci. USA.* 85:5946–5950.

Gundersen, G.G., E.R. Gomes, and Y. Wen. 2004. Cortical control of microtubule stability and polarization. *Curr. Opin. Cell Biol.* 16:106–112.

Hacker, U., R. Albrecht, and M. Maniak. 1997. Fluid-phase uptake by macropinocytosis in *Dictyostelium. J. Cell Sci.* 110:105–112.

Hammer, J.A., III, and G. Jung. 1996. The sequence of the *Dictyostelium* myo J heavy chain gene predicts a novel, dimeric, unconventional myosin with a heavy chain molecular mass of 258 kDa. *J. Biol. Chem.* 271:7120–7127.

Hawari, F.I., F.N. Rouhani, X. Cui, Z.X. Yu, C. Buckley, M. Kaler, and S.J. Levine. 2004. Release of full-length 55-kDa TNF receptor 1 in exosome-like vesicles: a mechanism for generation of soluble cytokine receptors. *Proc. Natl. Acad. Sci. USA.* 101:1297–1302.

Heijnen, H.F., A.E. Schiel, R. Fijnheer, H.J. Geuze, and J.J. Sixma. 1999. Activated platelets release two types of membrane vesicles: microvesicles by surface shedding and exosomes derived from exocytosis of multivesicular bodies and alpha-granules. *Blood.* 94:3791–3799.

Hintermann, R., and R.W. Parish. 1979. The intracellular location of adenylyl cyclase in the cellular slime molds *Dictyostelium discoideum* and *Polysphondylium pallidum. Exp. Cell Res.* 123:429–434.

Kimmel, A.R., and C.A. Parent. 2003. The signal to move: *D. discoideum* go orienteering. *Science.* 300:1525–1527.

Kriebel, P.W., and C.A. Parent. 2004. Adenylyl cyclase expression and regulation during the differentiation of *Dictyostelium discoideum. IUBMB Life.* 56:541–546.

Kriebel, P.W., V.A. Barr, and C.A. Parent. 2003. Adenylyl cyclase localization regulates streaming during chemotaxis. *Cell.* 112:549–560.

Kupfer, A., D. Louvard, and S.J. Singer. 1982. Polarization of the Golgi apparatus and the microtubule-organizing center in cultured fibroblasts at the edge of an experimental wound. *Proc. Natl. Acad. Sci. USA*. 79:2603–2607.

Laemmli, U.K. 1970. Cleavage of sructural proteins during the assembly of the head of bacteriophage T4. *Nature.* 227:680–685.

Maeda, Y., and G. Gerisch. 1977. Vesicle formation in *Dictyostelium discoideum* cells during oscillations of cAMP synthesis and release. *Exp. Cell Res.* 110:119–126.

Mayer, C., K. Maaser, N. Daryab, K.S. Zanker, E.B. Brocker, and P. Friedl. 2004. Release of cell fragments by invading melanoma cells. *Eur. J. Cell Biol.* 83:709–715.

Neujahr, R., R. Albrecht, J. Kohler, M. Matzner, J.M. Schwartz, M. Westphal, and G. Gerisch. 1998. Microtubule-mediated centrosome motility and the positioning of cleavage furrows in multinucleate myosin II-null cells. *J. Cell Sci.* 111:1227–1240.

Niggli, V. 2003. Microtubule-disruption-induced and chemotactic-peptide-induced migration of human neutrophils: implications for differential sets of signalling pathways. *J. Cell Sci.* 116:813–822.

Niswonger, M.L., and T.J. O'Halloran. 1997. Clathrin heavy chain is required for spore cell but not stalk cell differentiation in *Dictyostelium discoideum. Development.* 124:443–451.

O'Halloran, T.J., and R.G. Anderson. 1992. Clathrin heavy chain is required for pinocytosis, the presence of large vacuoles, and development in *Dictyostelium. J. Cell Biol.* 118:1371–1377.

Parent, C.A. 2004. Making all the right moves: chemotaxis in neutrophils and *Dictyostelium. Curr. Opin. Cell Biol.* 16:4–13.

Parent, C.A., and P.N. Devreotes. 1996a. Constitutively active adenylyl cyclase mutant requires neither G proteins nor cytosolic regulators. *J. Biol. Chem.* 271:18333–18336.

Parent, C.A., and P.N. Devreotes. 1996b. Molecular genetics of signal transduction in *Dictyostelium. Annu. Rev. Biochem.* 65:411–440.

Parent, C.A., B.J. Blacklock, W.M. Froehlich, D.B. Murphy, and P.N. Devreotes. 1998. G protein signaling events are activated at the leading edge of chemotactic cells. *Cell.* 95:81–91.

Peterson, M.D., A.S. Urioste, and M.A. Titus. 1996. *Dictyostelium discoideum* myoJ: a member of a broadly defined myosin V class or a class XI unconventional myosin? *J. Muscle Res. Cell Motil.* 17:411–424.

Polishchuk, R.S., E.V. Polishchuk, P. Marra, S. Alberti, R. Buccione, A. Luini, and A.A. Mironov. 2000. Correlative light-electron microscopy reveals the tubular-saccular ultrastructure of carriers operating between Golgi apparatus and plasma membrane. *J. Cell Biol.* 148:45–58.

Raposo, G., H.W. Nijman, W. Stoorvogel, R. Liejendekker, C.V. Harding, C.J. Melief, and H.J. Geuze. 1996. B lymphocytes secrete antigen-presenting vesicles. *J. Exp. Med.* 183:1161–1172.

Ratner, S., W.S. Sherrod, and D. Lichlyter. 1997. Microtubule retraction into the uropod and its role in T cell polarization and motility. *J. Immunol.* 159:1063–1067.

Reipert, S., I. Fischer, and G. Wiche. 2004. High-pressure freezing of epithelial cells on sapphire coverslips. *J. Microsc.* 213:81–85.

Ridley, A.J., M.A. Schwartz, K. Burridge, R.A. Firtel, M.H. Ginsberg, G. Borisy, J.T. Parsons, and A.R. Horwitz. 2003. Cell migration: integrating signals from front to back. *Science.* 302:1704–1709.

Ruscetti, T., J.A. Cardelli, M.L. Niswonger, and T.J. O'Halloran. 1994. Clathrin heavy chain functions in sorting and secretion of lysosomal enzymes in *Dictyostelium discoideum. J. Cell Biol.* 126:343–352.

Sasaki, A.T., C. Chun, K. Takeda, and R.A. Firtel. 2004. Localized Ras signaling at the leading edge regulates PI3K, cell polarity, and directional cell movement. *J. Cell Biol.* 167:505–518.

Taverna, S., G. Ghersi, A. Ginestra, S. Rigogliuso, S. Pecorella, G. Alaimo, F. Saladino, V. Dolo, P. Dell'Era, A. Pavan, et al. 2003. Shedding of membrane vesicles mediates fibroblast growth factor-2 release from cells. *J. Biol. Chem.* 278:51911–51919.

Thery, C., L. Zitvogel, and S. Amigorena. 2002. Exosomes: composition, biogenesis and function. *Nat. Rev. Immunol.* 2:569–579.

Uchida, K., and S. Yumura. 1999. Novel cellular tracks of migrating *Dictyostelium* cells. *Eur. J. Cell Biol.* 78:757–766.

Van Haastert, P.J., and P.N. Devreotes. 2004. Chemotaxis: signalling the way forward. *Nat. Rev. Mol. Cell Biol.* 5:626–634.

Vida, T.A., and S.D. Emr. 1995. A new vital stain for visualizing vacuolar membrane dynamics and endocytosis in yeast. *J. Cell Biol.* 128:779–792.

Wang, J., V.C. Virta, K. Riddelle-Spencer, and T.J. O'Halloran. 2003. Compromise of clathrin function and membrane association by clathrin light chain deletion. *Traffic.* 4:891–901.

Weiner, O.D., P.O. Neilsen, G.D. Prestwich, M.W. Kirschner, L.C. Cantley, and H.R. Bourne. 2002. A PtdInsP(3)- and Rho GTPase-mediated positive feedback loop regulates neutrophil polarity. *Nat. Cell Biol.* 4:509–513.

Wessels, D., J. Reynolds, O. Johnson, E. Voss, R. Burns, K. Daniels, E. Garrard, T.J. O'Halloran, and D.R. Soll. 2000. Clathrin plays a novel role in the regulation of cell polarity, pseudopod formation, uropod stability and motility in *Dictyostelium. J. Cell Sci.* 113:21–36.

Wu, X., X. Xiang, and J.A. Hammer III. 2006. Motor proteins at the microtubule plus-end. *Trends Cell Biol.* 16:135–143.

Xiao, Z., N. Zhang, D.B. Murphy, and P.N. Devreotes. 1997. Dynamic distribution of chemoattractant receptors in living cells during chemotaxis and persistent stimulation. *J. Cell Biol.* 139:365–374.

Xu, J., F. Wang, A. Van Keymeulen, M. Rentel, and H.R. Bourne. 2005. Neutrophil microtubules suppress polarity and enhance directional migration. *Proc. Natl. Acad. Sci. USA.* 102:6884–6889.

Yamaguchi, H., J. Wyckoff, and J. Condeelis. 2005. Cell migration in tumors. *Curr. Opin. Cell Biol.* 17:559–564.

Zhu, Q., and M. Clarke. 1992. Association of calmodulin and an unconventional myosin with the contractile vacuole complex of *Dictyostelium discoideum. J. Cell Biol.* 118:347–358.

Zitvogel, L., A. Regnault, A. Lozier, J. Wolfers, C. Flament, D. Tenza, P. Ricciardi-Castagnoli, G. Raposo, and S. Amigorena. 1998. Eradication of established murine tumors using a novel cell-free vaccine: dendritic cell-derived exosomes. *Nat. Med.* 4:594–600.